MIMO Communication Measurements in Small Cell Scenarios at 28 GHz

Joerg Eisenbeis, *Graduate Student Member, IEEE*, Magnus Tingulstad, Nicolai Kern, *Graduate Student Member, IEEE*, Zsolt Kollár, *Member, IEEE*, Jerzy Kowalewski, *Member, IEEE*, Pablo Ramos López, and Thomas Zwick, *Fellow, IEEE*

***Abstract*— Massive multiple-input–multiple-output (MIMO) systems operating in the centimeter-wave (cmWave) and millimeter-wave (mmWave) region offer huge spectral efficiencies, which enables to satisfy the urgent need for higher data rates in mobile communication networks. However, the proper design of those massive MIMO systems first requires a deep understanding of the underlying wireless propagation channel. Therefore, we present a fully digital MIMO measurement system operating around 28 GHz. The system enables to take fast subsequent snapshots of the complex MIMO channel matrix. Based on this method, we statistically analyze the time-dependent channel behavior, the achievable signal quality and spectral efficiency, as well as the channel eigenvalue profile. Furthermore, the presented calibration approach for the receiver enables an estimation of the dominant absolute angle of arrival (AoA) and allows us to draw conclusions about the line-of-sight (LOS) dominance of the scenario. In total, 159 communication measurements over 20 s are conducted in three different small cell site scenarios to investigate the wireless propagation behavior. The measurements reveal the existence of several spatial propagation paths between the mobile transmitter and the base station. Furthermore, an insight into their likelihood in different propagation scenarios is also given.**

***Index Terms*— Channel estimation, mobile communication, multiple-input–multiple-output (MIMO) communication.**

I. Introduction

MORE than ever before, mobile wireless communication networks demand for higher data rates. To meet these requirements, research and industry focus in particular on exploiting the large available spectral resources in the centimeter-wave (cmWave) and millimeter-wave (mmWave) region, the decrease of the cell size to increase the spectral reuse, and the utilization of MIMO systems to achieve a spatial multiplexing gain [1]–[5]. As the path losses increase with higher carrier frequencies, the application in mobile wireless communication networks is limited to small cell scenarios [6], [7]. Furthermore, at these higher frequencies, massive MIMO mobile radio base stations, employing large-scale antenna arrays with hundreds of antenna elements, are realizable in a compact form factor, offering huge spectral efficiencies [8]–[10]. These huge spectral efficiencies are achieved by transmitting uncorrelated data streams to the spatially separated users and exploiting the multipath channel between the mobile radio base station and each user to obtain a spatial multiplexing gain [11]. As a result, the Third Generation Partnership Project (3GPP) lately defined the n257-band between 26.5 and 29.5 GHz offering 3 GHz of spectral bandwidth [12].

To investigate the achievable data rates of massive MIMO communication systems in the n257-band and answer important system design questions, a deep understanding of the wireless propagation channel is required. Note that the propagation conditions determine the expected channel capacity of MIMO systems [13]. In practice, MIMO algorithms and architectures are evaluated in numerical simulations based on models of the wireless propagation channel [14]. Nevertheless, these channel models depend on simplifications of the complicated electromagnetic propagation and thereby never fully reproduce the propagation effects [15]. For these reasons, extensive measurement campaigns have to be performed to characterize the wireless propagation channel and demonstrators are needed to verify the performance and validate channel models.

A. Channel Measurements Around 28 GHz

Untill date, many research groups realized channel sounding systems to investigate the propagation characteristics around 28 GHz as presented in [16]–[46]. Particularly worthy to mention are the extensive measurement campaigns by Rappaport *et al.* [16] for the 28, 38, 60, and 73 GHz mmWave bands summarized. At 28 GHz, the results for urban scenarios reveal path loss exponents of 2.1 for line-of-sight (LOS) and 3.4 for nonline-of-sight (NLOS) scenarios, which are similar to today's microwave path loss models [16], [47], [48].

Another important research aspect in wireless channel sounding is the analysis of the dynamic channel behavior.

Manuscript received January 27, 2020; revised September 15, 2020; accepted November 9, 2020. Date of publication December 18, 2020; date of current version July 7, 2021. This work was supported in part by the Electronic Components and Systems for European Leadership (ECSEL) Joint Undertaking funded through H2020-EU.2.1.1.7. in the Framework of the TARANTO Project under Grant 737454, in part by the German Federal Ministry of Education under Grant 16ESE0211, and in part by the National Research, Development and Innovation (NRDI) Fund (based on the charter of bolster issued by the NRDI Office under the auspices of the Ministry for Innovation and Technology, Hungary). *(Corresponding author: Joerg Eisenbeis.)*

Joerg Eisenbeis, Magnus Tingulstad, Jerzy Kowalewski, Pablo Ramos López, and Thomas Zwick are with the Institute of Radio Frequency Engineering and Electronics (IHE), Karlsruhe Institute of Technology (KIT), 76131 Karlsruhe, Germany (e-mail: joerg.eisenbeis@kit.edu).

Nicolai Kern was with the Institute of Radio Frequency Engineering and Electronics (IHE), Karlsruhe Institute of Technology (KIT), 76131 Karlsruhe, Germany. He is now with the Institute of Microwave Engineering, Ulm University, 89081 Ulm, Germany.

Zsolt Kollár is with the Institute of Radio Frequency Engineering and Electronics (IHE), Karlsruhe Institute of Technology (KIT), 76131 Karlsruhe, Germany, and also with the Department of Measurement and Information Systems (MIT), Budapest University of Technology and Economics (BME), 1117 Budapest, Hungary.

Color versions of one or more figures in this article are available at https://doi.org/10.1109/TAP.2020.3044394.

Digital Object Identifier 10.1109/TAP.2020.3044394

Therefore, the required measurement times to acquire the channel characteristics at each transmitter and receiver location have to be reduced. To better temporally analyze the wireless propagation channel, Bas *et al.* [17], [49] presented an MIMO channel sounder at 28 GHz based on a phased array structure that performs fast beam steering. Compared to channel sounders with rotating horn antennas, the measurement time could drastically be reduced down to milliseconds [17]. The channel sounder is used to analyze the outdoor to indoor propagation channel in [50] and [51] and to estimate the angular spectrum, delay spread, and Doppler spectrum in an outdoor micro cellular scenario in [52]. A different approach reducing the channel measurement time is introduced by Tataria *et al.* [19]. The presented MIMO channel sounder measures the 256×128 dual-polarized channel by switching between the different elements. In contrast to previous works, snapshots of the MIMO channel can be acquired in 380 ms.

Beside the extensive channel characterization efforts made, first, MIMO demonstrators operating within the n257-band have been presented in the literature. Researchers from Samsung Electronics demonstrated in [53] first indoor and outdoor coverage tests using a subarray-based (subconnected) hybrid beamforming testbed. This work was extended in [54] achieving data rates of up to 7.5 Gb/s by transmitting four parallel data streams to two mobile stations in close distance. Recently, Yang *et al.* [55] reported the first fully digital massive MIMO transceiver operating at 28 GHz consisting of 64 antenna elements. In the demonstrator test, 20 noncoherent data streams could be transmitted at the same time to eight user entities resulting in spectral efficiency of 101.5 b/s/Hz. Furthermore, MIMO communication measurements are presented by NTT Docomo in [56]–[58].

B. Main Contributions

To tackle the problem of long measurement times of current channel sounders and analyze achievable communication data rates within realistic small cell scenarios, we present a fully digital 16×4 MIMO measurement system operating around 28 GHz. Unlike the channel sounders presented earlier, we analyze the wireless propagation behavior by estimating and evaluating subsequent snapshots of the complex MIMO channel matrix, representing the time-dependent channel response between each transmit and receive antenna assuming a frequency nonselective channel [59]. This method enables us to take snapshots of the channel in much less than a millisecond allowing a good analysis of the dynamic propagation behavior. The main contributions can be summarized as follows.

1) This work presents a method to rapidly acquire narrowband snapshots of the complex MIMO channel matrix, which enables us to investigate the wireless propagation behavior around 28 GHz.
2) We verify this approach and analyze the MIMO wireless propagation channel in a total of 159 measurements in three different small cell site scenarios. For each measurement, the mobile unit is placed at a different location and the received data are recorded for around 20 s. Snapshots of the MIMO channel are estimated for each symbol, i.e., each 128 μs.
3) A calibration approach for fully digital MIMO architectures is presented and implemented at the receiver allowing the correction of amplitude and phase imbalances between the receive branches. This facilitates the estimation of the dominant absolute angle of arrival (AoA). With simultaneous determination of the spatial positions of transmitter and receiver as well as the receiver orientation, the found AoA allows to draw conclusions about the LOS dominance of the scenario.
4) We present for the first time measurement results for the channel eigenvalue statistics around 28 GHz. This statistic reveals with which likelihood up to four spatial propagation paths can be utilized. Note that the eigenvalues of the channel determine whether spatial multiplexing (Blast-type) communication techniques are wise to be applied [11].
5) Furthermore, the subsequent snapshots of the MIMO channel matrix are used to evaluate the achievable spectral efficiencies. The measurement results give information about the degradation in spectral efficiency caused by foliage within the wireless propagation paths, as the coherence time is reduced.

It should be noted that our MIMO communication demonstrator does not aim to replace the current channel sounder, but rather serves as an complementary approach to analyze the so far insufficiently investigated channel characteristics, as, for example, the time-dependent eigenvalue profile of the channel. In advance, the measured snapshots of the channel matrix can be directly fed into measurement-based MIMO channel models, to numerically analyze novel MIMO communication architectures and algorithms [60], [61]. Note that new architectures and algorithms are mostly evaluated in numerical simulations utilizing abstract MIMO channel models as presented in [62]–[66].

This work is organized as follows. Section II presents the hardware setup as well as the methods for receiver calibration and channel estimation. In Section III, the outdoor measurement scenarios are described in detail. Finally, Section IV discusses the results of the channel analysis around 28 GHz.

II. MIMO Channel Measurement Approach

To investigate the behavior of the wireless propagation channel around 28 GHz, we developed a fully digital MIMO measurement system. The system is designed to measure the multipath channel characteristic emulating an uplink communication scenario between a mobile user with $M_{\text{ant}} = 4$ transmitters and a base station with $N_{\text{ant}} = 16$ receivers. In this section, we introduce the designed hardware setup and explain the developed channel estimation and system calibration approach. Furthermore, the estimation of the dominant AoA is explained and the modulation error ratio (MER) is discussed as a metric for assessing signal quality.

A. System Setup

The measurement system consists of a fully digital 16×4 MIMO configuration with four transmit antennas at the mobile

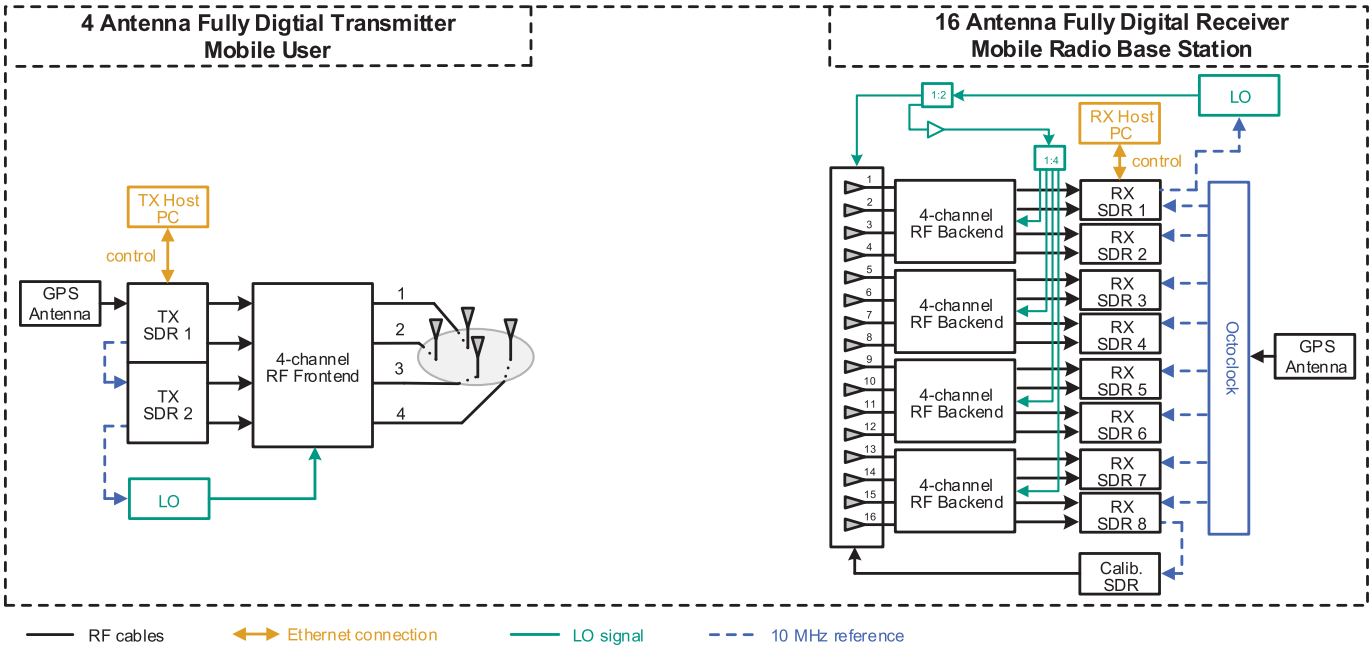

Fig. 1. Block diagram of the 16 × 4 MIMO channel sounder.

user entity and 16 receive antennas at the base station. The block diagram of the system configuration is shown in Fig. 1. To achieve a high sensitivity, a heterodyne architecture is selected, which enables a flexible adjustment of the radio frequency (RF) and intermediate frequency (IF).

1) Mobile Transmitter: At the transmitter side, the training signals for channel estimation are generated by a host computer (PC) connected via Gigabit-Ethernet to two commercial software-defined radios (SDRs) of type USRP X310 by Ettus Research. The SDRs include digital-to-analog-conversion, baseband-to-IF conversion, as well as IF filtering and amplification.

To translate the IF to the desired RF frequency band, an RF front end with four symmetrical transmit branches is designed. It consists of a four metal layer printed circuit board (PCB) with a substrate of type RO4003C from Rogers Corporation with a height of 203 μm and a dielectric constant $\varepsilon_r = 3.55$. The IF-to-RF conversion and RF amplification are realized by commercially available monolithic microwave integrated circuits (MMICs). The PCB is integrated into a metallic housing for electromagnetic shielding, protection, and better heat dissipation. The mixer includes an internal frequency doubler and the upper sideband of the mixing process is used, resulting in an RF center frequency

$$f_{\mathrm{RF}} = 2 f_{\mathrm{LO}} + f_{\mathrm{IF}} \tag{1}$$

where f_{IF} is the IF in the range of 400 MHz–3.5 GHz and f_{LO} is the externally supplied local oscillator (LO) frequency in the range 12–13.5 GHz depending on the selected IF. The RF can be set in the range of the n257-band between 26.5 and 29.5 GHz. For all inputs and outputs of the RF front-end module, 2.92 mm connectors are utilized. The RF front end is connected to the SDRs and the antenna via coaxial cables. The measured output 1 dB-compression point of the RF front end is 10 dBm.

For the mobile transmitter, four monopole antennas are mounted on a metallic housing to enable a 360° coverage in the azimuth plane. This makes the mobile transmitter independent of a rotation in azimuth. The monopole antennas have a height of $\lambda_0/4$ at 28 GHz to avoid dips in the elevation radiation pattern. In elevation, the measured half-power beamwidth (HPBW) is 26° with the main beam direction of 20.5° upward originating from the ground plane of the monopoles. The tilt by 20.5° upward is selected to be a good fit for the considered application scenario, where the base station is installed on an elevated position. The measured maximum realized element gain, including connector and feed line losses, is 1.5 dBi. The monopoles are arranged in a square separated by $0.55\lambda_0$ at 28 GHz to achieve uniform coverage in azimuth over the entire 360° range. If the antennas are not properly spaced, notches in the azimuth radiation pattern would occur.

For the later measurement campaign, the RF front end and SDRs are integrated within a transportable box and placed together with the DC power supply and LO signal generator on a trolley shown in Fig. 2(c).

2) Base Station: At the base station or receiver side, a 16 antenna element board is designed with an element spacing of 5.35 mm, which relates to a spacing of $\lambda_0/2$ at 28 GHz. All antenna elements are realized as microstrip patch antennas using the same four metal layer RO400C PCB as for the RF front end. To increase the antenna element gain, two serially fed microstrip patch elements are vertically stacked, narrowing down the HPBW in elevation direction to 40.8°. The HPBW in azimuth is 86°. The measured realized element gain, including the connector and feed line losses, is 4.1dBi. A photograph of the front of the antenna board is shown in Fig. 2(a).

The 16 RF outputs of the antenna board are connected via coaxial cables to four RF back ends each consisting of

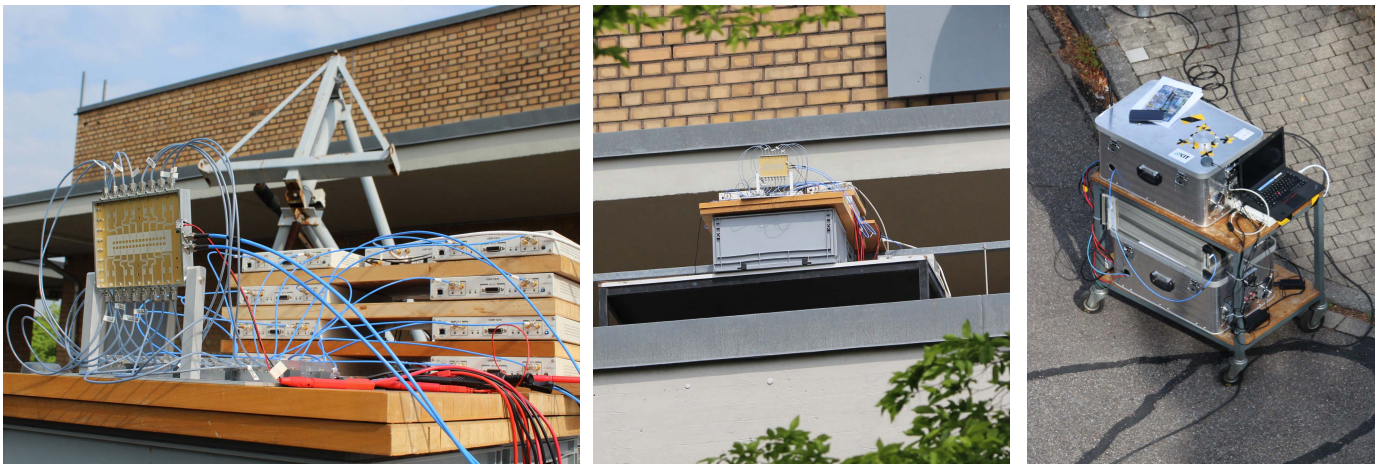

(a) (b) (c)

Fig. 2. Photographs of the base station and mobile transmitter setup. (a) Close-up photograph of the base station setup in the cell site scenario II. (b) View of the base station from the user's perspective. (c) Mobile transmitter setup as seen from the base station.

four symmetric channels performing low-noise amplification, bandpass filtering, and RF-to-IF conversion. The RF back ends are constructed according to the same scheme as for the RF front ends utilizing a four metal layer RO400C PCB, commercial available MMICs, 2.92 mm connectors, and a metal housing adapted to the PCB. Furthermore, the antenna board is mounted together with the RF back-end modules onto a metallic construction, which allows a manual adjustment of the antenna elevation angle. The LO signal for RF-to-IF downconversion is, similar to the transmitter side, supplied externally at half the mixing frequency to each RF front end, as shown in Fig. 1.

Finally, the received and digitized data are transferred via Ethernet to a host PC, where online and offline postprocessing is performed. The receiver noise figure (NF) is calculated based on the information given in the data sheets of the used components to NF $\approx$ 2.1 dB.

3) Transmitter and Receiver Clock and Frequency Synchronization: GPS-disciplined, oven-controlled crystal oscillators (GPSDOs) by Jackson Labs Technologies, Inc., in combination with active GPS antennas by Ettus Research are employed to synchronize the SDRs and LO signal generators at the transmitter and receiver sides. The GPSDOs provide a high-accuracy 10 MHz reference with a phase noise of -110 dBc/Hz at 10 Hz and a pulse-per-second (PPS) signal to ensure a synchronous sampling between the SDRs. The PPS signal is aligned to the global standard within 50 ns. At the transmitter, the GPSDO is integrated into the first SDR. The 10 MHz reference and PPS are forwarded from the first SDR via daisy chaining to the second SDR. Moreover, the 10 MHz reference is provided to the LO signal generator, as shown in Fig. 1. At the receiver, the GPSDO is integrated into a OctoClock-G CDA-2990 by Ettus Research. The OctoClock-G CDA-2990 has eight 10 MHz reference and PPS outputs that are connected to the SDRs at the receiver. The additional SDR for calibration receives the 10 MHz reference and PPS via daisy chaining. Furthermore, the 10 MHz reference is forwarded by the first SDR via daisy chaining to the LO signal generator at the receiver.

To allow a sufficiently long warm-up time and settling to the global reference, the GPSDOs are switched ON 1 h in advance of the measurements. For the presented measurements in this work, no frequency offset could be detected in the signals recorded at the receiver, which indicates a sufficiently precise global reference. The GPS coordinates provided in this process are also used in the later measurement campaigns to determine the spatial position of the transmitter and receiver.

B. Channel Estimation Principle and Signal Processing

To estimate the MIMO propagation channel, known training symbols are transmitted at the mobile user entity as it is standard in many communication systems [67], [68]. As signal waveform orthogonal frequency-division multiplexing (OFDM) is used. The randomly selected training symbols are modulated using quadrature-phase shift keying (QPSK). OFDM facilitates the separation of the different transmit antennas by using exclusive OFDM subcarriers and enables the estimation of the complex MIMO channel matrix with several measurement points in the frequency domain [69]. By separating the transmit antennas in the frequency domain, the transmitters can be separated at each receive antenna, realizing an estimation of the instantaneous complex MIMO channel matrix. The MIMO channel matrix represents the channel response between each transmit and receive antenna assuming a frequency nonselective channel [59]. To fulfill this assumption, the signal bandwidth has to be smaller than the coherence bandwidth [70]. This also motivates to utilize OFDM, as the frequency-nonselectivity assumption just needs to be true for the bandwidth of a small range of OFDM subcarriers.

Let $\mathcal{I} \in \{0, 1, \ldots, N_c - 1\}$ be an index set addressing the N_c OFDM subcarriers and divide it into a subset of indices $\mathcal{I}_d$, containing the complex modulated data symbols used for channel estimation purposes and a subset of indices $\mathcal{I}_0$, containing the positions of all null carriers. It holds

$$\mathcal{I}_d \,\dot{\cup}\, \mathcal{I}_0 = \mathcal{I}. \tag{2}$$

Furthermore, the subset $\mathcal{I}_0$ contains the indices of the subcarriers around zero frequency to avoid blockage due to high DC parts $\mathcal{I}_{\mathrm{DC}} \subseteq \mathcal{I}_0$, the indices of upper and lower guard carriers $\mathcal{I}_{\mathrm{guard}} \subseteq \mathcal{I}_0$, and further recessed OFDM subcarriers for receiver calibration $\mathcal{I}_{\mathrm{cal}} \subseteq \mathcal{I}_0$. Hence, no subcarrier index is part of two subsets, meaning that the sets are disjoint so that

$$\mathcal{I}_0 = \mathcal{I}_{\mathrm{DC}} \cup \mathcal{I}_{\mathrm{guard}} \cup \mathcal{I}_{\mathrm{cal}} \tag{3}$$

and

$$\mathcal{I}_{\mathrm{DC}} \cap \mathcal{I}_{\mathrm{guard}} \cap \mathcal{I}_{\mathrm{cal}} = \emptyset \tag{4}$$

is fulfilled. The transmit antennas are separated for the channel estimation process using exclusive OFDM subcarriers. Therefore, the index set $\mathcal{I}_d$ is divided into M_{ant} subsets $\mathcal{I}_{d,m} \subseteq \mathcal{I}_d$ with $m \in \{1, 2, \ldots, M_{\mathrm{ant}}\}$ containing the $|\mathcal{I}_{d,m}|$ exclusive subcarriers of the mth transmit antenna. It holds

$$\mathcal{I}_d = \dot{\bigcup}_{m=1}^{M_{\mathrm{ant}}} \mathcal{I}_{d,m}. \tag{5}$$

The OFDM subcarrier indices follow an interleaved assignment to the different transmit antennas to minimize the spacing between two neighboring subcarriers of one subset $\mathcal{I}_{d,m}$. The OFDM subcarrier spacing is defined as

$$\Delta f = B_s / N_c = 1 / T_{\mathrm{o}} \tag{6}$$

where B_s represents the available signal bandwidth and T_{o} is the OFDM symbol duration.

Based on the defined index sets, the complex OFDM data frame for one OFDM symbol in the frequency domain $\boldsymbol{X} \in \mathbb{C}^{M_{\mathrm{ant}} \times N_c}$ is constructed. The discrete OFDM time-domain signal with sampling time $t = q \cdot T_{\mathrm{o}}/N_c$ and $q \in \{0, 1, \ldots, N_c - 1\}$ can be written as [59], [71]

$$\boldsymbol{u}(m, q) = \sum_{p=0}^{N_c - 1} \boldsymbol{X}(m, p) \cdot e^{j2\pi pq/N_c} \tag{7}$$

where $p \in \{0, 1, \ldots, N_c - 1\}$ denotes the indices for the OFDM subcarrier frequencies $f_p = p \cdot \Delta f = p/T_{\mathrm{o}}$. The channel response of a multipath channel can be represented by [72], [73]

$$\boldsymbol{h}(n, m, q) = \sum_{d=0}^{N_p - 1} \boldsymbol{h}_c(n, m, d, q) \cdot \delta(q - d) \tag{8}$$

consisting of N_p replicas of the transmit signal arriving with the discrete delay time in samples d and complex weighting factor $\boldsymbol{h}_c(n, m, d, q)$ at the time sample point q at the receiver. For the received signal, following with the index set, $n \in \{0, 1, \ldots, N_{\mathrm{ant}} - 1\}$ of the receive antennas

$$\boldsymbol{y}(n, q) = \sum_{m=0}^{M_{\mathrm{ant}} - 1} \sum_{d=0}^{N_p - 1} \boldsymbol{h}_c(n, m, d, q) \cdot \boldsymbol{u}(m, q - d) + \boldsymbol{n}(n, q), \tag{9}$$

where $\boldsymbol{n} \in \mathbb{C}^{N_{\mathrm{ant}} \times N_c}$ accounts for the additive white Gaussian noise introduced during transmission. The multiplication of the transmit signals with a time-variant channel would lead to a cyclic convolution in frequency domain and thereby to intercarrier interferences (ICIs). To avoid ICI, the OFDM symbol duration has to be chosen smaller than the coherence time of the channel so that the complex channel coefficients $\boldsymbol{h}_c(n, m, d, q)$ can be assumed constant over one OFDM symbol. With this assumption, the received signal in the frequency or symbol domain results after discrete Fourier transformation (DFT) to

$$\boldsymbol{R}(n, p) = \sum_{m=0}^{M_{\mathrm{ant}} - 1} \sum_{d=0}^{N_p - 1} \mathrm{DFT}\{\boldsymbol{H}(n, m, d) \cdot \boldsymbol{u}(m, q - d)\} + \boldsymbol{N}(n, p). \tag{10}$$

To avoid intersymbol interferences (ISIs), the same OFDM symbol is transmitted continuously, thereby omitting the need for a guard interval. Due to the cyclic properties of the transmit sequence, the time shifting property of the DFT

$$\boldsymbol{u}(\cdot, q - d) \circ\!\!-\!\!\bullet\, \boldsymbol{X}(\cdot, p) \cdot e^{-j2\pi qd/N_c} \tag{11}$$

can be exploited, leading to

$$\begin{aligned} \boldsymbol{R}(n, p) &= \sum_{m=0}^{M_{\mathrm{ant}} - 1} \sum_{d=0}^{N_p - 1} \boldsymbol{H}(n, m, d) \boldsymbol{X}(m, p) e^{-j2\pi pd/N_c} + \boldsymbol{N}(n, p) \\ &= \sum_{m=0}^{M_{\mathrm{ant}} - 1} \tilde{\boldsymbol{H}}(n, m) \boldsymbol{X}(m, p) + \boldsymbol{N}(n, p) \end{aligned} \tag{12}$$

with the channel frequency response

$$\tilde{\boldsymbol{H}}(n, m) = \sum_{d=0}^{N_p - 1} \boldsymbol{H}(n, m, d) e^{-j2\pi pd/N_c}. \tag{13}$$

At the receiver, the channel can be estimated using the least squares estimation [74]

$$\hat{\boldsymbol{H}}_{\mathrm{f}}(n, p) = \boldsymbol{R}(n, p) \cdot \boldsymbol{T}(p)^{-1} \tag{14}$$

with the known transmit data symbols

$$\boldsymbol{T}(p) = \sum_{m=0}^{M_{\mathrm{ant}} - 1} \boldsymbol{X}(m, p). \tag{15}$$

As the transmitters are separated by their OFDM subcarriers defined in $\mathcal{I}_{d,m}$, the MIMO channel matrix can be estimated to

$$\hat{\boldsymbol{H}}(n, m) = \frac{1}{|\mathcal{I}_{d,m}|} \sum_{p \in \mathcal{I}_{d,m}} \hat{\boldsymbol{H}}_{\mathrm{f}}(n, p) \tag{16}$$

averaging over all subcarrier of each transmitter assuming a frequency nonselective channel for the full signal bandwidth $B_s = N_c \cdot \Delta f$. It is therefore necessary that the receiver knows the training symbols as well as the OFDM subcarrier indices of the individual transmitters $\mathcal{I}_{d,m} \forall m$.

C. System Calibration and AoA Estimation

An important achievement of the hardware design is the determination of the strongest absolute AoA at the receiver. This requires a correction of the imbalances in amplitude and phase between the 16 RF receive branches, which results

from cable length deviations, manufacturing tolerances of the PCBs and MMICs, deviations in soldering, and phase differences of the LO signals. Especially, the used SDRs cause a random phase offset between the branches because there is no possibility to harmonize the phase of the LO signals for IF upconversion and downconversion. Therefore, a calibration branch was added to the hardware design to correct these imbalances. The calibration branch consists of an additional SDR at the receiver generating the calibration signal, which is fed at the IF to a dedicated input port of the receiver antenna board. The receiver antenna board incorporates a mixer that upconverts the calibration signal to RF using an externally supplied LO signal at half the mixing frequency, as shown in Fig. 1. The calibration signal is then split symmetrically by a distribution network and added to the receive signal directly behind the 16 antenna elements using a coupled-line directional coupler. As the calibration signal is known at the receiver and is symmetrically coupled into each receive path, the relative differences between the amplification and phase of the receive branches can be estimated and corrected in the digital domain of the receiver. The amplitude and phase imbalances have to be only corrected with respect to a selected receiver branch. It is important to mention that to enable a real-time calibration, the received and calibration signals have to be separated to avoid interference. This separation is achieved by keeping selected OFDM carriers of the transmitted signal free for the calibration signal. As defined before, the OFDM subcarrier calibration index set is denoted by $\mathcal{I}_{\text{cal}}$ and it holds $\mathcal{I}_{\text{cal}} \cap \mathcal{I}_d = \emptyset$. The introduced imbalances are measured for each OFDM symbol in the same manner as in (14) resulting in

$$\hat{d}_n = \frac{1}{|\mathcal{I}_{\text{cal}}|} \sum_{p \in \mathcal{I}_{\text{cal}}} \tilde{\boldsymbol{R}}(n, p) \cdot \boldsymbol{C}(n)^{-1}, \tag{17}$$

where $\tilde{\boldsymbol{R}}$ represents the received baseband signal matrix, including the superimposed calibration signal. Finally, the result is used to obtain the calibrated MIMO channel matrix

$$\hat{\boldsymbol{H}}_{\text{cal}} = \hat{\boldsymbol{D}}^{-1} \cdot \hat{\boldsymbol{H}} \tag{18}$$

with the calibration matrix $\hat{\boldsymbol{D}} = \text{diag}\{\hat{d}_0, \ldots, \hat{d}_{N_{\text{ant}}-1}\}$.

Based on the calibrated channel matrix, the strongest AoA $\hat{\phi}_{\max}$ can be determined. Therefore, the singular value decomposition (SVD) of the calibrated channel matrix is calculated $\hat{\boldsymbol{H}}_{\text{cal}} = \hat{\boldsymbol{U}} \hat{\boldsymbol{\Sigma}} \hat{\boldsymbol{V}}^H$ to extract the first receiver-side beamforming vector $\hat{\boldsymbol{u}}_1 \in \mathbb{C}^{N_{\text{ant}} \times 1}$ of $\hat{\boldsymbol{U}} = [\hat{\boldsymbol{u}}_1^T, \ldots, \hat{\boldsymbol{u}}_{N_{\text{ant}}}^T]^T$. The radiation pattern over the azimuth angle ϕ using the first receiver-side beamforming vector results to

$$\boldsymbol{C}(\phi) = \sum_{n=0}^{N_{\text{ant}}-1} \hat{\boldsymbol{u}}_1^H(n) \boldsymbol{C}_{\text{e}}(n, \phi) e^{jk\vec{\boldsymbol{d}}(n) \sin\phi} \tag{19}$$

where $\hat{\boldsymbol{u}}_1^H$ denotes the Hermitian transpose of $\hat{\boldsymbol{u}}_1$, $\boldsymbol{C}_{\text{e}}$ contains the antenna element characteristics, $k = 2\pi/\lambda$ denotes the wavenumber, and $\vec{d}$ represents a vector with the spatial positions of the active antenna elements. As the first receiver-side beamforming vector enables a beam steering into the direction of the strongest AoA, the corresponding angle can be extracted by finding the maximum in the radiation pattern. The strongest AoA is, therefore, given by

$$\hat{\phi}_{\max} = \arg\max_{\phi} \{|\boldsymbol{C}(\phi)|\} \tag{20}$$

which can be compared with the physical azimuth angle between the position of the base station and the mobile transmitter ϕ_{bt}. The angle ϕ_{bt} can be calculated using the GPS coordinates of the base station and the mobile transmitter with respect to the view direction of the base station. The angular difference

$$\Delta\phi = |\phi_{\text{bt}} - \hat{\phi}_{\max}| \tag{21}$$

equals zero for scenarios with a dominant LOS path but can have an arbitrary value for NLOS scenarios. This means that the angular difference $\Delta\phi$ can give information about whether the scenario is LOS dominated. In principle, multiple AoAs can be extracted from the estimated and calibrated channel matrix, by analyzing the radiation characteristic, including all beamforming vectors given by $\hat{\boldsymbol{U}}^H$.

D. Signal Quality and Performance Metrics

As a measure of the signal quality, the MER representing a quasi-signal-to-noise ratio (SNR) is calculated. Before estimating the MER, the received symbols are equalized assuming a frame-based data transmission with frame length L_{f} with periodic appearing training symbols as it is common practice in wireless communications [75]. A one tap equalization is applied using as an equalization matrix

$$\boldsymbol{\Lambda} = \frac{1}{L_{\text{f}}} \sum_{k=0}^{L_{\text{f}}-1} \hat{\boldsymbol{H}}_{\text{f}}(\cdot, \cdot, k) \tag{22}$$

where $\hat{\boldsymbol{H}}_{\text{f}} \in \mathbb{C}^{N_{\text{ant}} \times N_c \times L_{\text{f}}}$ is the result of (14) extended in time domain with sampling times $t = k \cdot T_{\text{o}}$ for $k \in \{0, 1, \ldots, L_{\text{f}} - 1\}$. On the basis of the equalized receive symbols $\boldsymbol{R}_{\text{eq}} \in \mathbb{C}^{N_{\text{ant}} \times N_c \times L_{\text{f}}}$, the MER averaged over all receivers and all OFDM carriers is defined by

$$\text{MER} = 10 \cdot \log_{10} \left\{ \frac{\sum_{p=0}^{N_c-1} \boldsymbol{P}_{\text{ref}}(p)}{\frac{1}{N_{\text{ant}} L_{\text{f}}} \sum_{n=1}^{N_{\text{ant}}} \sum_{p=0}^{N_c-1} \sum_{k=0}^{L_{\text{f}}-1} \boldsymbol{E}(n, p, k)} \right\} \tag{23}$$

with the error matrix

$$\begin{aligned} \boldsymbol{E}(n, p, k) = {} & [\text{Re}\{\boldsymbol{T}(p)\} - \text{Re}\{\boldsymbol{R}_{\text{eq}}(n, p, k)\}]^2 \\ & + [\text{Im}\{\boldsymbol{T}(p)\} - \text{Im}\{\boldsymbol{R}_{\text{eq}}(n, p, k)\}]^2 \end{aligned} \tag{24}$$

and the normalization matrix

$$\boldsymbol{P}_{\text{ref}}(p) = \text{Re}\{\boldsymbol{T}(p)\}^2 + \text{Im}\{\boldsymbol{T}(p)\}^2 \tag{25}$$

following the descriptions in [76]. Furthermore, the MER can be averaged over $L_s = \lfloor L_{\text{tot}}/L_{\text{f}} \rfloor$ subsequent OFDM frames, where L_{tot} represents the total number of recorded OFDM symbols.

As a performance metric serves the spectral efficiency or maximum achievable sum rate given in b/s/Hz and calculated by [77]

$$R = \log_2 \left\{ \left| \boldsymbol{I}_{N_{\text{ant}}} + \frac{\gamma}{M_{\text{ant}}} \hat{\boldsymbol{H}} \hat{\boldsymbol{H}}^H \right| \right\} \tag{26}$$

with the normalized channel matrix $||\hat{\boldsymbol{H}}||^2 = N_{\text{ant}} M_{\text{ant}}$. For the SNR at the receiver γ, we use the calculated MER in the following analysis.

III. Outdoor Measurement Scenarios

For the channel measurements, we selected three different cell site scenarios to obtain a realistic picture of the wireless propagation channel. The scenarios were chosen due to their variability in foliage coverage, reflective surfaces, denseness of buildings, availability of LOS and NLOS measurement points, and their angular spread. Within each scenario, we positioned the base station at an elevated position with a fixed view direction and elevation angle. The position of the mobile transmitter is varied within a predesignated measurement area seen from the base station view direction, making an analysis of the different propagation scenarios and view angles to the base station possible. The determination of the exact spatial position of the transmitter and receiver is based on the recorded and over the measurement period averaged GPS data that are manually verified using a map of the scenario. The 50 channels GPS receiver by Jackson Labs Technologies, Inc., provides regarding the manufacturer a measured horizontal position accuracy of better than 0.7 m (root-mean-square value) utilizing a low-cost vehicle puck antenna operated on the roof of a building without any high adjacent buildings blocking the view. For each measurement position of the mobile transmitter, an around 20 s long recording is made. This allows us to analyze the time-dependent behavior of the channel, as, for example, the influence of foliage movement within the propagation paths. In total, 159 measurements are performed and evaluated. The measurements are performed on several days from May to July causing a high amount of foliage within the surrounding area. During the measurements, the weather was partly cloudy and dry. Three different small cell site scenarios were picked for comparison at Campus South of the Karlsruhe Institute of Technology (KIT). For each cell site scenario, the elevation and azimuth view direction of the base station is adjusted upfront to cover the desired area best possible. The scenarios are marked in the satellite image in Fig. 3. The image shows the respective position of the base station (B_1, B_2, and B_3), their view directions (i.e., the normal vectors to the antenna array plane), and the angular ranges of $\pm 60^\circ$ around the view directions. The different cell sites can be described as follows.

1) Scenario I: In the first scenario, the base station is adjusted to cover an open courtyard, which is characterized by a small lake surrounded by buildings on its three sides serving as possible reflective surfaces. Furthermore, a fair amount of foliage belonging to tall trees in the center of the courtyard was present. These blocked a direct LOS propagation between the base station and the mobile transmitter at some of the measurement locations, which shows a significant impact on the SNR. At the furthermost end of the courtyard, two small building canyons run on either side of a building, possibly creating highly reflective environments. In addition, some parked cars prevented the direct LOS path. The base station is positioned on the balcony of an adjacent building in 13 m height, and the antenna array is tilted downward in elevation by 12° from the horizontal view direction.

TABLE I
Overview of the Cell Site Parameters

	Scenario I	Scenario II	Scenario III
Base station height	13 m	17 m	35 m
Tilt in elevation	12°	15°	28°
No. of measurements	49	62	48
Min. distance	28 m	22 m	49 m
Max. distance	99 m	124 m	162 m
Max. azimuth angle	64.5°	92.1°	61.4°

2) Scenario II: The second scenario covers an intersection and is dominated by heavy foliage spread over a wide angular range, as shown on the right side of the satellite image in Fig. 3. The base station is thereby placed on the roof top of a building in 17 m height and tilted in elevation by 15° downward from the horizontal view direction. The heavy foliage coverage is blocking the LOS path at multiple measurement locations, giving possibility to further investigate the influences of foliage onto the propagation channel. Compared with the first cell site scenario, a less reflective environment is present, with a wide street running through the scenario lined by trees and parked cars. Furthermore, occasional wind present on the day of measurement introduced time-variant scattering effects due to movements of the foliage during the measurement times.

3) Scenario III: In the third scenario, the base station is placed on a balcony in 35 m height and the antenna array is tilted downward in elevation by 28° from the horizontal view direction. This scenario comprises few trees, which in combination with the base station height is leading to measurement distances up to 162 m. Here, urban NLOS propagation scenarios are present at several measurement locations.

The key figures of the different cell site scenarios are summarized in Table I. To enable a realistic mobile communication scenario, the antennas of the mobile transmitter are placed in a height of 115 cm in all scenarios to emulate the typical height of a cell phone carried by a user. Moreover, the height of the base stations is chosen following the urban micro and macro cell scenarios with high user density identified by 3GPP in [78]. Due to a maximum distance of 162 m within the measurements, the atmospheric gap around 28 GHz and the absence of rain during our measurements, the additional atmospheric path losses can be neglected [79].

IV. Channel Measurement Results

In Section III, the results of the channel measurements are presented. The system parameters used for our measurements are given in Table II. The considerably narrow bandwidth is selected to ensure a frequency-nonselective channel behavior. It should be noted that the presented measurements focus on estimating snapshots of the complex MIMO channel matrix. For more information about the broadband channel behavior or other characteristics as, for example, power delay profiles, we refer to the measurement results presented in [16], [18],

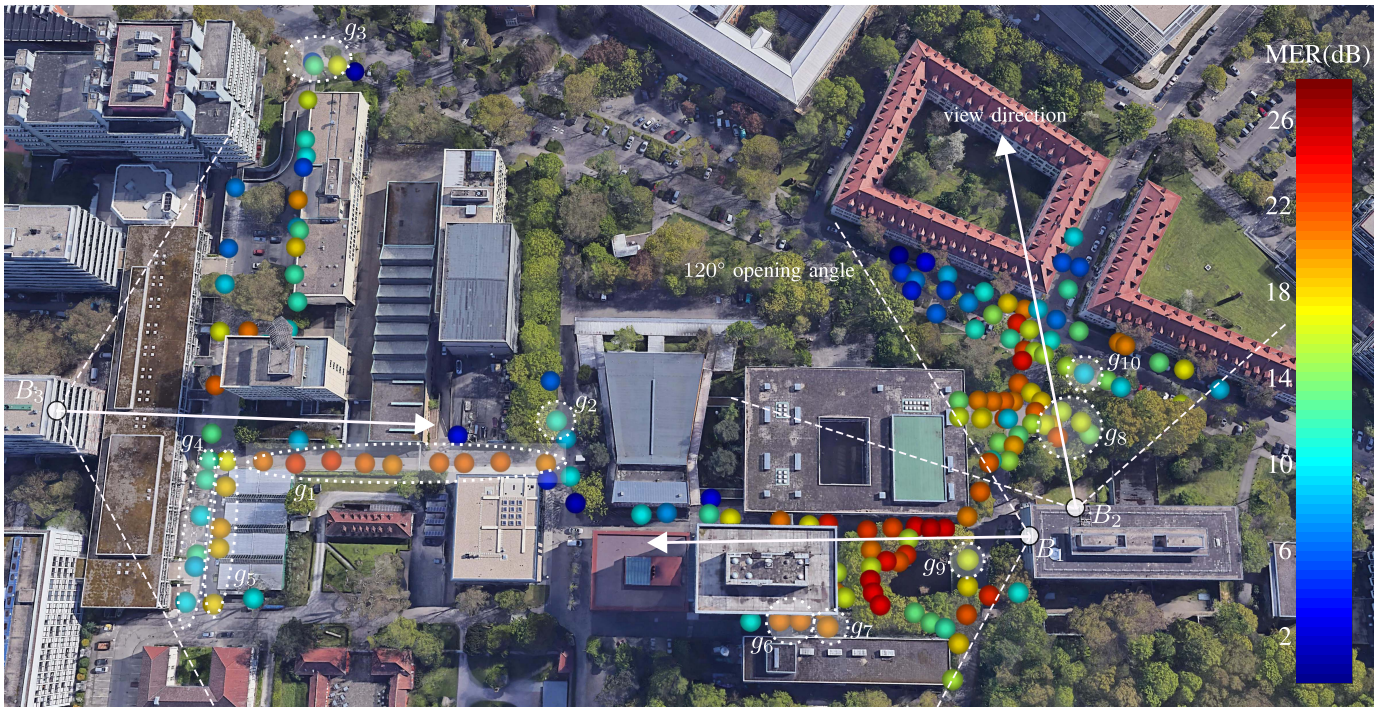

Fig. 3. Satellite image of the measurement cell site scenarios at KIT Campus South. For the base station positions (B_1, B_2, and B_3) marked as white circles, the view direction of the antenna array as well as an azimuth opening angle of 120° is drawn into the picture. Furthermore, the estimated average MER over the whole recording is color-encoded shown for each position of the mobile transmitter. The cell site scenarios cover LOS as well as NLOS scenarios, azimuth angles of over 60°, and distances up to 162 m. The measurements reveal the suitability of buildings as reflectors and the influence of vegetation onto the measurements. For better reference, parts of the measurement locations are grouped by semitransparent white dashed lines and indexed as $\{g_1, g_2 \ldots, g_{10}\}$. Image source: Google Earth 2019 GeoBasis-DE/BKG.

TABLE II
MEASUREMENT SYSTEM PARAMETERS

Parameter	Symbol	Value
MIMO size	$N_{\text{ant}} \times M_{\text{ant}}$	16×4
RF frequency	f_{RF}	27.8 GHz
IF	f_{IF}	2.46 GHz
Transmit power	P_{Tx}	10 dBm
Tx antenna element gain	G_{Tx}	1.5 dBi
Rx antenna element gain	G_{Rx}	4.1 dBi
Estimated receiver noise figure	NF	2.1 dB
Sampling frequency	f_s	1 MSps
Frame length	L_{f}	10
FFT size	N_c	128 points
OFDM subcarrier spacing	$\Delta f = f_s/N_c$	7.8125 kHz
Number of allocated carriers	$\lvert\mathcal{I}_d\rvert$	80
Number of calibration carriers	$\lvert\mathcal{I}_{\text{cal}}\rvert$	10
Number of DC null carriers	$\lvert\mathcal{I}_{\text{DC}}\rvert$	5
Number of guard carriers	$\lvert\mathcal{I}_{\text{guard}}\rvert$	33
OFDM symbol duration	T_{o}	128 µs
Digital modulation scheme		QPSK

[50], [52], and [80]. Nevertheless, it is generally possible to use the demonstrator for broadband channel measurements as the designed RF front ends cover the full n257-band. For this purpose, the IF frequency can be varied in time by controlling the utilized SDRs, and thus, a wide frequency range can be investigated. However, this presupposes a stationary channel over the entire measurement. The modular design also allows the replacement of the bandwidth limiting antennas and SDRs by analog-to-digital converter (ADC) and digital-to-analog converter (DAC) boards with higher sampling rates and processing speeds.

At first, the average MER over the full recording is calculated for each transmitter position and color-coded displayed into Fig. 3. The results show that the MER varies strongly depending on the position of the mobile transmitter. This is caused by the high number of trees in the propagation paths, which leads to large path losses at 28 GHz. For good propagation scenarios MER values of up to 26 dB could be reached. These values are achieved without using any antenna array gain, i.e., an equivalent isotropically radiated power (EIRP) of 11.5 dBm, due to the employed channel estimation technique. The MER values, therefore, look quite promising for future 28 GHz MIMO mobile communication systems. As expected, the highest values could be reached in short distance LOS scenarios at or close to the view direction of the base station. The group of measurement locations marked as g_1 in Fig. 3 shows multiple LOS measurements with different distances between the base station and the mobile transmitter ranging from 64 m to 150 m. The elevation angle decreases thereby from 33° to 13°, and furthermore, the transmitter moves away from the base station. The measurements show that the MER only slightly decreases with distance, as a lower elevation angle between the base station and the mobile transmitter leads to a higher antenna element gain at the transmitter

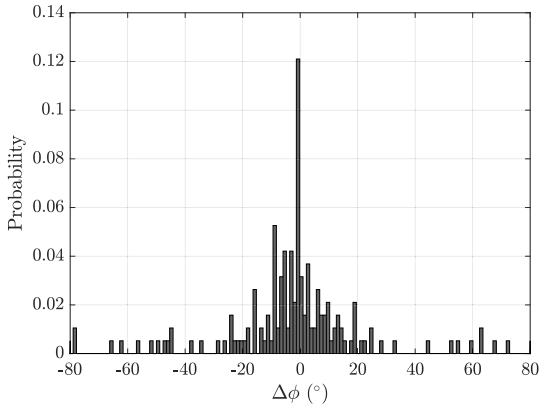

Fig. 4. Statistic of the angular difference $\Delta\phi$ between the physical azimuth angle and the main azimuth beam direction over all mobile transmitter positions in all three cell site scenarios.

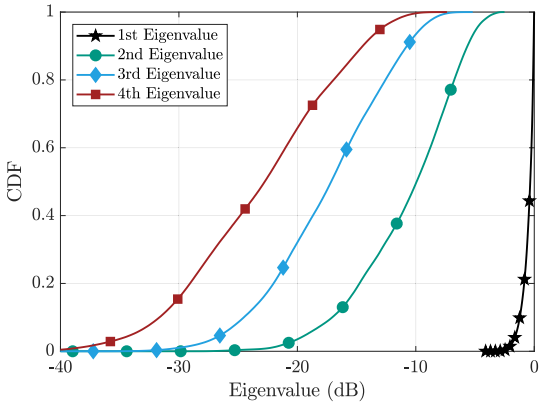

Fig. 5. Cumulative distribution function of the normalized eigenvalues of the channel including all mobile transmitter locations of all cell site scenarios.

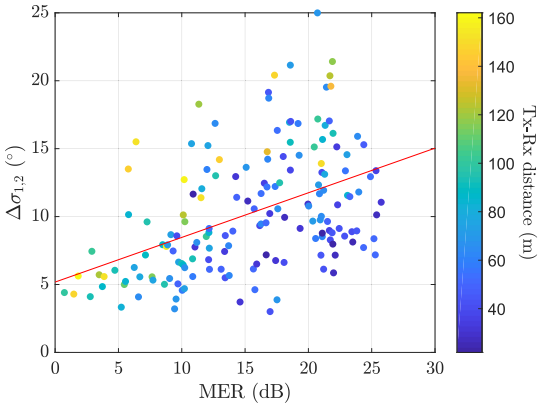

Fig. 6. Difference between the first and second eigenvalues of the channel $\Delta\sigma_{1,2}$ versus the average MER. The distance between the base station receiver and the mobile transmitter is color-encoded into the graph.

and receiver side. Moreover, foliage losses can be estimated using the furthermost point of g_1 and comparing it with the measurement position of g_2. Note that a slight difference in distance for both locations has only a minor impact on the path loss and thereby MER. The measurements show a difference in MER of 9.5 dB due to foliage in the LOS path. Measurement group g_3 indicates that the MIMO system can successfully operate within a high angular range in azimuth of above 60° achieving MER values of up to 17 dB. The measurement positions summarized in g_4 have no direct LOS connection to the base station, as the mobile transmitter was shadowed by the adjacent building. Interesting is the comparison with the measurement positions in g_5 made on the other side of the street enabling an LOS connection. The difference in MER between both groups is roughly 8.5 dB, showing the stronger path loss of NLOS propagation scenarios. Nevertheless, the difference in MER in the NLOS connection of measurement position g_6 and the LOS connection of measurement position g_7 is only 0.2 dB. This low loss in the NLOS case results from high building fronts surrounding the mobile transmitter like a canyon, which enables the propagation toward the base station. The high influence of the vegetation-like trees and bushes onto the path loss can be shown in group g_8, where a high number of spatially close measurements have been made showing a high range of MER values varying between 16 and 22 dB.

To analyze whether the wireless propagation channel is LOS or NLOS dominant, the histogram of the angular difference $\Delta\phi$ calculated by (21) is shown in Fig. 4, including all mobile transmitter positions. The result shows an LOS dominance within the measurements made. The reasons for this are not only the selection of the mobile transmitter locations but also the fact that the likelihood for multipath propagation decreases compared to frequencies below 6 GHz. This is caused by the higher path losses and absorption by possible reflectors. Besides the peak around $\Delta\phi = 0°$, the angular difference is spread over the whole range. Note that due to the limited number of measurements, not every angular difference is present in Fig. 4.

To analyze the multipath nature of the wireless propagation channel in detail, Fig. 5 shows the cumulative distribution function (CDF) of the four eigenvalues of the channel, including all mobile transmitter locations of all cell site scenarios. The graph reveals the multipath nature of the wireless propagation channel. It can be seen that even in this LOS dominated cell site scenarios in 50% of the cases, the second eigenvalue is not more than 10 dB lower than the strongest one. Moreover, in 10% of the cases, the difference between the strongest and weakest eigenvalue is less than 14 dB.

For a deeper understanding of the multipath behavior of the 28 GHz propagation channel, taking a closer look at the difference between the first and second eigenvalue $\Delta\sigma_{1,2}$ is of interest. In Fig. 6, the eigenvalue difference is plotted over the MER for all locations of the mobile transmitter. The eigenvalue difference is averaged in time over the full recording. Furthermore, the distance between the base station and the mobile transmitter is color-encoded onto the measurement points. Fig. 6 shows that for low MER values, the differences between the first and second eigenvalues of the channel are low. This can be explained by the type of scenario causing the low MER. These scenarios mostly have no LOS connection and the distance between the base station and mobile transmitter is comparably high, as shown by the color-encoded points. Hence, if no dominant path exists, the difference between the eigenvalues most likely decreases. Going to higher MER values, the difference in the eigenvalues seems to increase in average as indicated by the trend line. This is mainly caused

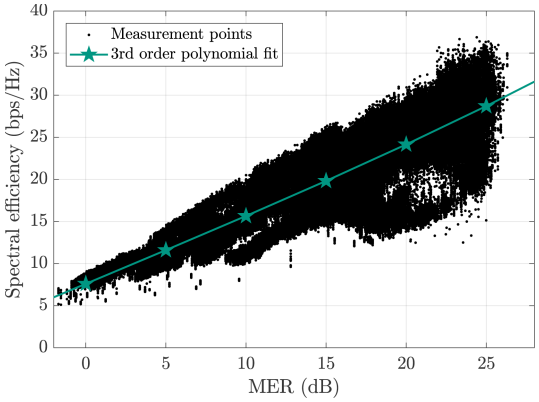

Fig. 7. Statistic of the achievable spectral efficiency versus the average MER for all mobile transmitter measurement locations of all cell site scenarios. The tendency of the measured spectral efficiency is illustrated using a third-order polynomial.

by LOS scenarios, as reflections over, e.g., buildings are much higher attenuated compared to the direct path. At medium to high values of the MER, all distances are represented supporting the thesis of LOS dominance. Furthermore, the results reveal that at medium and high MER values, the distance between the eigenvalues decreases predominantly if the distance between the base station and mobile transmitter is low. This means that at closer distances, multipath scenarios exist, which can be exploited for spatial multiplexing or diversity transmission.

To investigate the achievable spectral efficiency in the presented mobile communication scenarios, the spectral efficiency for all mobile transmitter positions and all scenarios is shown in Fig. 7. In addition, the course of the spectral efficiency is approximated as a third-order polynomial function using the measurement data. While the spectral efficiency increases with an increasing MER, the uncertainty also rises. This behavior is in line with the observations made in Fig. 6. For high MER values, the scenario may have only one dominant LOS path leading to a low spectral efficiency, as only the first eigenvalue contributes to the transmission. The spectral efficiency, in this case, is dominated by the eigenvalue distribution. At low MER values, all eigenvalues are highly attenuated, which means that the spectral efficiency is dominated by the MER. As, for wider bandwidths, additional frequency-selective distortions will reduce the signal quality, the presented results of the narrowband achievable spectral efficiency can be used as an indicator for the reachable performance. This helps designers of broadband communication systems to put the achieved spectral efficiency into perspective and indicates the amount of additional interference caused by broadband data transmission.

Next, the time-dependent behavior of the propagation channel is analyzed. For this, the beamforming matrices resulting from SVD may be applied to time-delayed instances of the channel matrix. Note that in real communication scenarios, the channel estimate is used during the transmission of the full frame until the channel estimation is updated, utilizing noncontinuous channel estimation approaches. This processing is valid as long as the coherence time is much larger than the frame duration or channel estimation update time. To evaluate the time-dependent behavior, the CDF of the

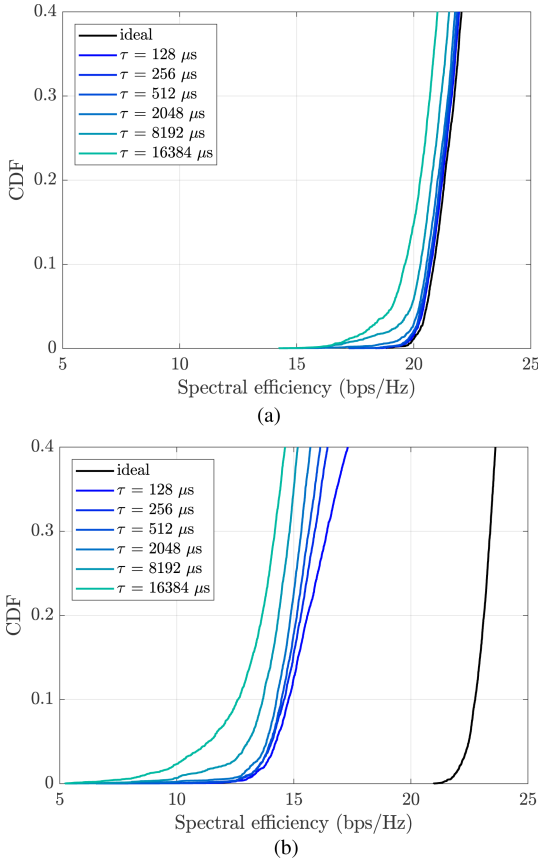

Fig. 8. Comparison of wireless propagation channels using the CDF of the spectral efficiency. To analyze the behavior over time, the calculated beamforming matrices were applied over several channel matrices delayed with τ. (a) Measurement location marked as g_9 within Fig. 3 showing a slow-changing wireless propagation channel meaning a long coherence time. (b) Measurement location marked as g_{10} within Fig. 3 showing a fast-changing wireless propagation channel meaning a short coherence time.

spectral efficiency is calculated for a slow- and fast-changing environment shown in Fig. 8. In each case, different frame durations given in multiples of the OFDM symbol duration are used. Note that as the channel is changing, the employed outdated beamforming matrix could also lead to an improvement in spectral efficiency. This is caused by a general improvement of the eigenvalues or MER occurring over time. To illustrate the loss in spectral efficiency by using a time-delayed beamforming matrix, the spectral efficiency is calculated for each channel matrix with delayed versions of the beamforming matrices. This indicates the difference between the time-delayed beamforming matrix and the optimum spectral efficiency, which can be reached at this point in time. Note that the minimum delay time is limited by the OFDM symbol duration $T_o = 128\,\mu$s. For a scenario with a long coherence time, we selected the measurement point marked as g_9 within Fig. 3. The communication link is dominated by an LOS connection with an average MER of 16.7 dB and no foliage between the base station and the mobile transmitter. The results in Fig. 8(a) show a slow degradation in spectral efficiency with increasing estimation delay. This means that the channel is changing slowly over time. Even for a high delay time of $\tau = 16.2$ ms, a drop in spectral efficiency of only 1.2 b/s/Hz is reached in 90% of the cases. In contrast, the

measurement point marked as g_{10} within Fig. 3 is analyzed, showing an average MER of 9.3 dB. Within this propagation scenario, the LOS path is covered by dense foliage, which rapidly changed the channel over time due to motions of leaves from the wind present that day. The difference is visualized in Fig. 8(b). Already, after $\tau = 128\,\mu$s, the wireless propagation channel and thereby the ideal beamforming matrix changed drastically leading to a drop of 8 b/s/Hz in 90% of the cases. Nevertheless, a saturation effect is visible caused by the static nonvariant parts in the propagation environment.

V. Conclusion

This work presents a measurement-based analysis of the wireless propagation channel around 28 GHz using an MIMO measurement system. Overall, 159 channel measurements at static mobile transmitter positions have been performed in three realistic small cell site scenarios. The spatial diversity of the channel is analyzed, showing less than 10 dB attenuation of the second path in 50% of the cases, which shows the possibility for spatial multiplexing techniques in future mobile communication scenarios at the edge of the mmWave regime. Moreover, the significant influences of moving foliage are investigated and their effects on the achievable spectral efficiency indicate the constraints for data frame durations. The channel sounder enables an estimation of the complex MIMO channel matrix, which can be fed into numerical simulations to investigate MIMO architectures and algorithms.

Acknowledgment

The authors thank A. Lipp, A. Gallego, M. Nonnenmacher, and R. Vester for their excellent support in building up the demonstrator.

References

[1] J. G. Andrews *et al.*, "What will 5G be?" *IEEE J. Sel. Areas Commun.*, vol. 32, no. 6, pp. 1065–1082, Jun. 2014.

[2] H. Viswanathan and M. Weldon, "The past, present, and future of mobile communications," *Bell Labs Tech. J.*, vol. 19, pp. 8–21, Aug. 2014.

[3] A. L. Swindlehurst, E. Ayanoglu, P. Heydari, and F. Capolino, "Millimeter-wave massive MIMO: The next wireless revolution?" *IEEE Commun. Mag.*, vol. 52, no. 9, pp. 56–62, Sep. 2014.

[4] A. Goldsmith, S. A. Jafar, N. Jindal, and S. Vishwanath, "Capacity limits of MIMO channels," *IEEE J. Sel. Areas Commun.*, vol. 21, no. 5, pp. 684–702, Jun. 2003.

[5] M. Xiao *et al.*, "Millimeter wave communications for future mobile networks," *IEEE J. Sel. Areas Commun.*, vol. 35, no. 9, pp. 1909–1935, Sep. 2017.

[6] H. Yan, S. Ramesh, T. Gallagher, C. Ling, and D. Cabric, "Performance, power, and area design trade-offs in millimeter-wave transmitter beamforming architectures," *IEEE Circuits Syst. Mag.*, vol. 19, no. 2, pp. 33–58, May 2019.

[7] R. Baldemair *et al.*, "Ultra-dense networks in millimeter-wave frequencies," *IEEE Commun. Mag.*, vol. 53, no. 1, pp. 202–208, Jan. 2015.

[8] X. Gao, O. Edfors, F. Rusek, and F. Tufvesson, "Massive MIMO performance evaluation based on measured propagation data," *IEEE Trans. Wireless Commun.*, vol. 14, no. 7, pp. 3899–3911, Jul. 2015.

[9] S. A. Busari, K. M. S. Huq, S. Mumtaz, L. Dai, and J. Rodriguez, "Millimeter-wave massive MIMO communication for future wireless systems: A survey," *IEEE Commun. Surveys Tuts.*, vol. 20, no. 2, pp. 836–869, 2nd Quart., 2018.

[10] E. Björnson, E. G. Larsson, and T. L. Marzetta, "Massive MIMO: Ten myths and one critical question," *IEEE Commun. Mag.*, vol. 54, no. 2, pp. 114–123, Feb. 2016.

[11] S. Sun, T. Rappaport, R. Heath, A. Nix, and S. Rangan, "MIMO for millimeter-wave wireless communications: Beamforming, spatial multiplexing, or both?" *IEEE Commun. Mag.*, vol. 52, no. 12, pp. 110–121, Dec. 2014.

[12] *Technical Specification Group Radio Access Network; New Frequency Range for NR (24.25-29.5 GHz) (Release 15), V1.0.0*, document ETSI TR 138 912 V15.0.0 (2018-09), RTR/TSGR-0038912vf00, 3GPP, Jun. 2018. [Online]. Available: https://www.etsi.org/deliver/etsi_tr/138900_138999/138912/15.00.00_60/tr_138912v150000p.pdf

[13] K. Yu and B. Ottersten, "Models for MIMO propagation channels: A review," *Wireless Commun. Mobile Comput.*, vol. 2, no. 7, pp. 653–666, Nov. 2002.

[14] T. S. Rappaport, Y. Xing, G. R. MacCartney, A. F. Molisch, E. Mellios, and J. Zhang, "Overview of millimeter wave communications for fifth-generation (5G) wireless networks—With a focus on propagation models," *IEEE Trans. Antennas Propag.*, vol. 65, no. 12, pp. 6213–6230, Dec. 2017.

[15] R. S. Thomä, D. Hampicke, A. Richter, G. Sommerkorn, and U. Trautwein, "MIMO vector channel sounder measurement for smart antenna system evaluation," *Eur. Trans. Telecommun.*, vol. 12, no. 5, pp. 427–438, Sep. 2001.

[16] T. S. Rappaport, G. R. MacCartney, M. K. Samimi, and S. Sun, "Wideband millimeter-wave propagation measurements and channel models for future wireless communication system design," *IEEE Trans. Commun.*, vol. 63, no. 9, pp. 3029–3056, Sep. 2015.

[17] C. U. Bas *et al.*, "Real-time millimeter-wave MIMO channel sounder for dynamic directional measurements," *IEEE Trans. Veh. Technol.*, vol. 68, no. 9, pp. 8775–8789, Sep. 2019.

[18] G. R. MacCartney and T. S. Rappaport, "A flexible millimeter-wave channel sounder with absolute timing," *IEEE J. Sel. Areas Commun.*, vol. 35, no. 6, pp. 1402–1418, Jun. 2017.

[19] H. Tataria, E. L. Bengtsson, P. C. Karlsson, O. Edfors, and F. Tufvesson, "Design and implementation aspects of a 28 GHz channel sounder for dynamic propagation characterization," in *Proc. 11th MC Meeting 11th Tech. Meeting Inclusive Radio Commun. Netw. 5G Beyond (IRACON)*. European Cooperation in Science and Technology (COST) Action CA15104, Sep. 2019.

[20] C. Gentile *et al.*, "Millimeter-wave channel measurement and modeling: A NIST perspective," *IEEE Commun. Mag.*, vol. 56, no. 12, pp. 30–37, Dec. 2018.

[21] S. Hur, Y.-J. Cho, J. Lee, N.-G. Kang, J. Park, and H. Benn, "Synchronous channel sounder using horn antenna and indoor measurements on 28 GHz," in *Proc. IEEE Int. Black Sea Conf. Commun. Netw. (BlackSeaCom)*, May 2014, pp. 83–87.

[22] S. Hur *et al.*, "Wideband spatial channel model in an urban cellular environments at 28 GHz," in *Proc. 9th Eur. Conf. Antennas Propag. (EuCAP)*, 2015, pp. 1–5.

[23] S. Hur *et al.*, "Proposal on millimeter-wave channel modeling for 5G cellular system," *IEEE J. Sel. Topics Signal Process.*, vol. 10, no. 3, pp. 454–469, Apr. 2016.

[24] S. Hur *et al.*, "Feasibility of mobility for millimeter-wave systems based on channel measurements," *IEEE Commun. Mag.*, vol. 56, no. 7, pp. 56–63, Jul. 2018.

[25] Z. Wen *et al.*, "MmWave channel sounder based on COTS instruments for 5G and indoor channel measurement," in *Proc. IEEE Wireless Commun. Netw. Conf.*, Apr. 2016, pp. 1–7.

[26] P. B. Papazian, K. A. Remley, C. Gentile, and N. Golmie, "Radio channel sounders for modeling mobile communications at 28 GHz, 60 GHz and 83 GHz," in *Proc. Global Symp. Millimeter-Waves (GSMM)*, May 2015, pp. 1–3.

[27] O. H. Koymen, A. Partyka, S. Subramanian, and J. Li, "Indoor mm-wave channel measurements: Comparative study of 2.9 GHz and 29 GHz," in *Proc. IEEE Global Commun. Conf. (GLOBECOM)*, Dec. 2015, pp. 1–6.

[28] J. Ryu, A. Partyka, S. Subramanian, and A. Sampath, "Study of the indoor millimeter wavelength channel," in *Proc. IEEE Global Commun. Conf. (GLOBECOM)*, Dec. 2015, pp. 1–6.

[29] J. Lee, J. Liang, J.-J. Park, and M.-D. Kim, "Directional path loss characteristics of large indoor environments with 28 GHz measurements," in *Proc. IEEE 26th Annu. Int. Symp. Pers., Indoor, Mobile Radio Commun. (PIMRC)*, Aug. 2015, pp. 2204–2208.

[30] H.-K. Kwon, M.-D. Kim, and Y.-J. Chong, "Implementation and performance evaluation of mmWave channel sounding system," in *Proc. IEEE Int. Symp. Antennas Propag., USNC/URSI Nat. Radio Sci. Meeting*, Jul. 2015, pp. 1011–1012.

[31] R. Müller, R. Herrmann, D. A. Dupleich, C. Schneider, and R. S. Thoma, "Ultrawideband multichannel sounding for mm-wave," in *Proc. 8th Eur. Conf. Antennas Propag. (EuCAP)*, Apr. 2014, pp. 817–821.

[32] T. Nakamura, A. Benjebbour, Y. Kishiyama, S. Suyama, and T. Imai, "5G radio access: Requirements, concept and experimental trials," *IEICE Trans. Commun.*, vol. E98.B, no. 8, pp. 1397–1406, 2015.

[33] X. Yin, C. Ling, and M.-D. Kim, "Experimental multipath-cluster characteristics of 28-GHz propagation channel," *IEEE Access*, vol. 3, pp. 3138–3150, 2015.

[34] M. Lei, J. Zhang, T. Lei, and D. Du, "28-GHz indoor channel measurements and analysis of propagation characteristics," in *Proc. IEEE 25th Annu. Int. Symp. Pers., Indoor, Mobile Radio Commun. (PIMRC)*, Sep. 2014, pp. 208–212.

[35] X. Wu, Y. Zhang, C. X. Wang, G. Goussetis, E. H. M. Aggoune, and M. M. Alwakeel, "28 GHz indoor channel measurements and modelling in laboratory environment using directional antennas," in *Proc. 9th Eur. Conf. Antennas Propag. (EuCAP)*, 2015, pp. 1–5.

[36] C. Larsson, F. Harrysson, B.-E. Olsson, and J.-E. Berg, "An outdoor-to-indoor propagation scenario at 28 GHz," in *Proc. 8th Eur. Conf. Antennas Propag. (EuCAP)*, Apr. 2014, pp. 3301–3304.

[37] J. Huang, R. Feng, J. Sun, C.-X. Wang, W. Zhang, and Y. Yang, "Multi-frequency millimeter wave massive MIMO channel measurements and analysis," in *Proc. IEEE Int. Conf. Commun. (ICC)*, May 2017, pp. 1–6.

[38] M. M. Lodro, N. Majeed, A. A. Khuwaja, A. H. Sodhro, and S. Greedy, "Statistical channel modelling of 5G mmWave MIMO wireless communication," in *Proc. Int. Conf. Comput., Math. Eng. Technol. (iCoMET)*, Mar. 2018, pp. 1–5.

[39] J. Hejselbaek, Y. Ji, W. Fan, and G. F. Pedersen, "Channel sounding system for MM-wave bands and characterization of indoor propagation at 28 GHz," *Int. J. Wireless Inf. Netw.*, vol. 24, no. 3, pp. 204–216, Sep. 2017.

[40] T. Jiang, L. Tian, P. Tang, Z. Hu, and J. Zhang, "Basestation 3-dimensional spatial propagation characteristics in urban microcell at 28 GHz," in *Proc. 11th Eur. Conf. Antennas Propag. (EUCAP)*, Mar. 2017, pp. 3167–3171.

[41] L. Zhou, L. Xiao, J. Li, Z. Yang, J. Lian, and S. Zhou, "Path loss model based on cluster at 28GHz in the office and corridor environments," in *Proc. IEEE 84th Veh. Technol. Conf. (VTC-Fall)*, Sep. 2016, pp. 1–5.

[42] S. Dahal, M. Faulkner, H. King, and S. Ahmed, "27.1 GHz millimetre wave propagation measurements for 5G urban macro areas," in *Proc. IEEE 85th Veh. Technol. Conf. (VTC Spring)*, Jun. 2017, pp. 1–5.

[43] P. Zhang, J. Li, H. Wang, and W. Hong, "Measurement-based propagation characteristics at 28 GHz and 39 GHz in suburban environment," in *Proc. IEEE Int. Symp. Antennas Propag. USNC-URSI Radio Sci. Meeting*, Jul. 2019, pp. 2121–2122.

[44] J.-H. Lee, J.-S. Choi, and S.-C. Kim, "Cell coverage analysis of 28 GHz millimeter wave in urban microcell environment using 3-D ray tracing," *IEEE Trans. Antennas Propag.*, vol. 66, no. 3, pp. 1479–1487, Mar. 2018.

[45] R. Naderpour, J. Vehmas, S. Nguyen, J. Jarvelainen, and K. Haneda, "Spatio-temporal channel sounding in a street canyon at 15, 28 and 60 GHz," in *Proc. IEEE 27th Annu. Int. Symp. Pers., Indoor, Mobile Radio Commun. (PIMRC)*, Sep. 2016, pp. 1–6.

[46] Y. Liu, L. Lin, and R. Zhang, "MIMO channel sounder and millimeter wave measurements in a conference room," in *Proc. 11th Int. Symp. Antennas, Propag. EM Theory (ISAPE)*, Oct. 2016, pp. 812–814.

[47] G. R. Maccartney, T. S. Rappaport, M. K. Samimi, and S. Sun, "Millimeter-wave omnidirectional path loss data for small cell 5G channel modeling," *IEEE Access*, vol. 3, pp. 1573–1580, 2015.

[48] G. R. MacCartney, M. K. Samimi, and T. S. Rappaport, "Omnidirectional path loss models in new york city at 28 GHz and 73 GHz," in *Proc. IEEE 25th Annu. Int. Symp. Pers., Indoor, Mobile Radio Commun. (PIMRC)*, Sep. 2014, pp. 227–231.

[49] C. U. Bas *et al.*, "A real-time millimeter-wave phased array MIMO channel sounder," in *Proc. IEEE Veh. Technol. Conf.*, no. 1, Sep. 2017, pp. 1–6.

[50] C. U. Bas *et al.*, "Outdoor to indoor propagation channel measurements at 28 GHz," *IEEE Trans. Wireless Commun.*, vol. 18, no. 3, pp. 1477–1489, Mar. 2019.

[51] C. U. Bas *et al.*, "Outdoor to indoor penetration loss at 28 GHz for fixed wireless access," in *Proc. IEEE Int. Conf. Commun. (ICC)*, May 2018, pp. 1–6.

[52] C. U. Bas *et al.*, "Dynamic double directional propagation channel measurements at 28 GHz–invited paper," in *Proc. IEEE 87th Veh. Technol. Conf. (VTC Spring)*, Jun. 2018, pp. 1–6.

[53] W. Roh *et al.*, "Millimeter-wave beamforming as an enabling technology for 5G cellular communications: Theoretical feasibility and prototype results," *IEEE Commun. Mag.*, vol. 52, no. 2, pp. 106–113, Feb. 2014.

[54] Y. Kim *et al.*, "Feasibility of mobile cellular communications at millimeter wave frequency," *IEEE J. Sel. Topics Signal Process.*, vol. 10, no. 3, pp. 589–599, Apr. 2016.

[55] B. Yang, Z. Yu, J. Lan, R. Zhang, J. Zhou, and W. Hong, "Digital beamforming-based massive MIMO transceiver for 5G millimeter-wave communications," *IEEE Trans. Microw. Theory Techn.*, vol. 66, no. 7, pp. 3403–3418, Jul. 2018.

[56] T. Obara, Y. Inoue, Y. Aoki, S. Suyama, J. Lee, and Y. Okumurav, "Experiment of 28 GHz band 5G super wideband transmission using beamforming and beam tracking in high mobility environment," in *Proc. IEEE 27th Annu. Int. Symp. Pers., Indoor, Mobile Radio Commun. (PIMRC)*, Sep. 2016, pp. 1–5.

[57] J. Mashino, K. Satoh, S. Suyama, Y. Inoue, and Y. Okumura, "5G experimental trial of 28 GHz band super wideband transmission using beam tracking in super high mobility environment," in *Proc. IEEE 85th Veh. Technol. Conf. (VTC Spring)*, Jun. 2017, pp. 1–5.

[58] D. Kurita *et al.*, "Outdoor experiments on 5G radio access using distributed MIMO and beamforming in 28-GHz frequency band," in *Proc. IEEE 28th Annu. Int. Symp. Pers., Indoor, Mobile Radio Commun. (PIMRC)*, Oct. 2017, pp. 1–6.

[59] J. Proakis and M. Salehi, *Digital Communications*, 5th ed. New York, NY, USA: McGraw-Hill, 2008.

[60] J. Eisenbeis, N. Kern, M. Tingulstad, L. G. de Oliveira, and T. Zwick, "Sparse array channel estimation for subarray-based hybrid beamforming systems," *IEEE Wireless Commun. Lett.*, early access, Sep. 18, 2020, doi: 10.1109/LWC.2020.3025171.

[61] J. Eisenbeis *et al.*, "Hybrid beamforming analysis based on MIMO channel measurements at 28 GHz," *TechRxiv*, Jul. 2020, doi: 10.36227/techrxiv.12639467.v1.

[62] A. Alkhateeb, G. Leus, and R. W. Heath, Jr., "Limited feedback hybrid precoding for multi-user millimeter wave systems," *IEEE Trans. Wireless Commun.*, vol. 14, no. 11, pp. 6481–6494, Nov. 2015.

[63] X. Gao, L. Dai, S. Han, C.-L. I, and R. W. Heath, Jr., "Energy-efficient hybrid analog and digital precoding for mmWave MIMO systems with large antenna arrays," *IEEE J. Sel. Areas Commun.*, vol. 34, no. 4, pp. 998–1009, Apr. 2016.

[64] N. N. Moghadam, G. Fodor, M. Bengtsson, and D. J. Love, "On the energy efficiency of MIMO hybrid beamforming for millimeter-wave systems with nonlinear power amplifiers," *IEEE Trans. Wireless Commun.*, vol. 17, no. 11, pp. 7208–7221, Nov. 2018.

[65] D. Zhang, Y. Wang, X. Li, and W. Xiang, "Hybridly connected structure for hybrid beamforming in mmWave massive MIMO systems," *IEEE Trans. Commun.*, vol. 66, no. 2, pp. 662–674, Feb. 2018.

[66] J. Eisenbeis, T. Mahler, P. R. Lopez, and T. Zwick, "Channel estimation method for subarray based hybrid beamforming systems employing sparse arrays," *Prog. Electromagn. Res. C*, vol. 87, pp. 25–38, Sep. 2018.

[67] L. Tong, B. M. Sadler, and M. Dong, "Pilot-assisted wireless transmissions–general model, design criteria, and signal processing," *IEEE Signal Process. Mag.*, vol. 21, no. 6, pp. 12–25, Nov. 2004.

[68] T. Zwick, T. J. Beukema, and H. Nam, "Wideband channel sounder with measurements and model for the 60 GHz indoor radio channel," *IEEE Trans. Veh. Technol.*, vol. 54, no. 4, pp. 1266–1277, Jul. 2005.

[69] T. Mahler, J. Kowalewski, B. Nub, C. Richt, J. Mayer, and T. Zwick, "Channel measurement based antenna synthesis for mobile automotive MIMO communication systems," *Prog. Electromagn. Res. B*, vol. 72, pp. 1–16, Jan. 2017.

[70] B. Sklar, "Rayleigh fading channels in mobile digital communication systems. II. Mitigation," *IEEE Commun. Mag.*, vol. 35, no. 7, pp. 102–109, Jul. 1997.

[71] M. Morelli, C.-C.-J. Kuo, and M.-O. Pun, "Synchronization techniques for orthogonal frequency division multiple access (OFDMA): A tutorial review," *Proc. IEEE*, vol. 95, no. 7, pp. 1394–1427, Jul. 2007.

[72] M. R. Raghavendra and K. Giridhar, "Improving channel estimation in OFDM systems for sparse multipath channels," *IEEE Signal Process. Lett.*, vol. 12, no. 1, pp. 52–55, Jan. 2005.

[73] O. Edfors, M. Sandell, J.-J. van de Beek, S. K. Wilson, and P. O. Borjesson, "OFDM channel estimation by singular value decomposition," in *Proc. Veh. Technol. Conf. (VTC)*, vol. 2, 1996, pp. 923–927.

[74] T. Hwang, C. Yang, G. Wu, S. Li, and G. Ye Li, "OFDM and its wireless applications: A survey," *IEEE Trans. Veh. Technol.*, vol. 58, no. 4, pp. 1673–1694, May 2009.

[75] H. Arslan and G. E. Bottomley, "Channel estimation in narrowband wireless communication systems," *Wireless Commun. Mobile Comput.*, vol. 1, no. 2, pp. 201–219, 2001.

[76] *Digital Video Broadcasting (DVB); Measurement Guidelines for DVB Systems*, Standard RTR/JTC-DVB-77, V1.2.1, European Telecommunications Standards Institute, May 2001.
[77] S. Loyka and G. Levin, "On physically-based normalization of MIMO channel matrices," *IEEE Trans. Wireless Commun.*, vol. 8, no. 3, pp. 1107–1112, Mar. 2009.
[78] "Technical specification group radio access network; Study on 3D channel model for LTE (release 12), V12.7.0," 3GPP, 3rd Generation Partnership Project, Tech. Rep. 3GPP TR 36.873 V12.7.0 (2017-12), Dec. 2014. [Online]. Available: https://www.3gpp.org/ftp/Specs/archive/36_series/36.873
[79] T. S. Rappaport *et al.*, "Millimeter wave mobile communications for 5G cellular: It will work!" *IEEE Access*, vol. 1, pp. 335–349, 2013.
[80] Y. Azar *et al.*, "28 GHz propagation measurements for outdoor cellular communications using steerable beam antennas in New York City," in *Proc. IEEE Int. Conf. Commun. (ICC)*, Jun. 2013, pp. 5143–5147.

Joerg Eisenbeis (Graduate Student Member, IEEE) received the B.Sc. and M.Sc. degrees in electrical engineering and information technology from the Karlsruhe Institute of Technology (KIT), Karlsruhe, Germany, in 2012 and 2014, respectively, where he is currently pursuing the Dr.Ing. (Ph.D.E.E.) degree with the Institute of Radio Frequency Engineering and Electronics.

Since 2015, he has been a Research Associate with the Institute of Radio Frequency Engineering and Electronics, KIT. His research focuses on hybrid beamforming communication systems, multiple-input–multiple-output (MIMO) wireless communications at millimeter-wave (mmWave) frequencies, and broadband satellite communication systems.

Mr. Eisenbeis received the TESAT RAUMFAHRTPREIS 2015 awarded by the German Association for Aerospace for his master's thesis entitled Systemsimulationen von Breitbandkommunikationssystemen im *E*-Band.

Magnus Tingulstad received the B.Sc. degree from RWTH Aachen University, Aachen, Germany, in 2017, and the M.Sc. degree from the Karlsruhe Institute of Technology, Karlsruhe, Germany, in 2019.

He currently works at Telenor ASA (Norwegian telecommunications company), Fornebu, Norway.

Nicolai Kern (Graduate Student Member, IEEE) received the M.Sc. degree in electrical engineering from the Karlsruhe Institute of Technology, Karlsruhe, Germany, in 2019. He is currently pursuing the Ph.D. degree with the Institute of Microwave Engineering, Ulm University, Ulm, Germany.

His research interests include machine learning applications in radar and radar sensor network signal processing.

Zsolt Kollár (Member, IEEE) received the Diploma and Ph.D. degrees in electric engineering from the Budapest University of Technology and Economics, Budapest, Hungary, in 2008 and 2013, respectively.

He was a Visiting Researcher with the Karlsruhe Institute of Technology (KIT), Karlsruhe, Germany, from October 2018 to April 2019. He is currently an Associate Professor with the Department of Measurement and Information Systems (MIT), Budapest University of Technology and Economics, where he is also the Head of the MATLAB laboratory. His research interests are digital signal processing, wireless communication, and quantization issues.

Jerzy Kowalewski (Member, IEEE) received the B.Sc. degree from the Gdansk University of Technology, Gdańsk, Poland, in 2011, and the M.Sc. degree in electrical engineering and the Dr.Ing. degree from the Karlsruhe Institute of Technology (KIT), Karlsruhe, Germany, in 2013 and 2020, respectively. (Ph.D.E.E.) degree with the Institute of Radio Frequency Engineering and Electronics.

His main research topic is reconfigurable antennas with a focus on pattern reconfiguration. His further interests are antennas for communication applications, UWB antennas, and wireless propagation topics.

Pablo Ramos López received the B.Sc. degree in electrical engineering and information technology from the Karlsruhe Institute of Technology (KIT), Karlsruhe, Germany, in 2018, where he is currently pursuing the degree with the Department of Electrical Engineering and Information Technology, KIT.

From June 2018 to August 2019, he worked as a Student Research Assistant with the Institute of Radio Frequency Engineering and Electronics (IHE), KIT.

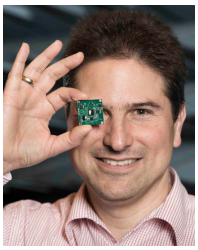

Thomas Zwick (Fellow, IEEE) received the Dipl.Ing. and Dr.Ing. degrees from the Universität Karlsruhe (TH), Karlsruhe, Germany, in 1994 and 1999, respectively.

In February 2001, he joined IBM as a Research Staff Member at the IBM T. J. Watson Research Center, Yorktown Heights, NY, USA. From October 2004 to September 2007, he was with Siemens AG, Lindau, Germany, managing the RF development team for automotive radars. In October 2007, he became a Full Professor at the Karlsruhe Institute of Technology (KIT), Karlsruhe, Germany, where he is also the Director of the Institute of Radio Frequency Engineering and Electronics.